Current relaxation due to hot carrier scattering in graphene

Dong Sun[1,5]**, Charles Divin**[1]**, Momchil Mihnev**[1]**, Torben Winzer**[2]**, Ermin Malic**[2]**, Andreas Knorr**[2]**, John E Sipe**[3]**, Claire Berger**[4]**, Walt A de Heer**[4]**, Phillip N First**[4] **and Theodore B Norris**[1,6]

[1] Center for Ultrafast Optical Science, University of Michigan, Ann Arbor, MI 48109-2099, USA
[2] Institut für Theoretische Physik, Technische Universität Berlin, 10623 Berlin, Germany
[3] Department of Physics and Institute for Optical Sciences, University of Toronto, ON M5S 1A7, Canada
[4] School of Physics, Georgia Institute of Technology, Atlanta, GA 30332, USA
[5] International Center for Quantum Materials, Peking University, 100871 Beijing, People's Republic of China
E-mail: tnorris@eecs.umich.edu

Abstract. In this paper, we present direct time-domain investigations of the relaxation of electric currents in graphene due to hot carrier scattering. We use coherent control with ultrashort optical pulses to photoinject a current and detect the terahertz (THz) radiation emitted by the resulting current surge. We pre-inject a background of hot carriers using a separate pump pulse, with a variable delay between the pump and current-injection pulses. We find the effect of the hot carrier background is to reduce the current and hence the emitted THz radiation. The current damping is determined simply by the density (or temperature) of the thermal carriers. The experimental behavior is accurately reproduced in a microscopic theory, which correctly incorporates the nonconservation of

[6] Author to whom any correspondence should be addressed.

velocity in scattering between Dirac fermions. The results indicate that hot carriers are effective in damping the current, and are expected to be important for understanding the operation of high-speed graphene electronic devices.

[S] Online supplementary data available from stacks.iop.org/NJP/14/105012/mmedia

When charge carriers in electronic materials collide, the net carrier energy and momentum are conserved. In conventional semiconductor materials having parabolic bands, such as GaAs with carriers near the gamma point, momentum conservation leads to current (velocity) conservation for scattering of carriers with the same effective mass (e.g. between electrons in the conduction band); scattering between carriers of different masses (e.g. between electrons and holes) leads to current relaxation [1–6]. The situation is quite different for materials in which the charge carriers are Dirac fermions as in grapheme [7, 8] or topological insulators [9–11]; in this case, momentum conservation does not imply current (velocity) conservation even for carriers of the same mass. It has been theoretically predicted that electron–electron scattering can lead to a reduction in low-field mobility and velocity saturation for steady-state transport in grapheme [6]. This unconventional transport behavior may have a profound impact on the performance of electronic and optoelectronic devices based on Dirac fermionic materials [12, 13]. For example, although the high mobility of graphene promises superior transport devices [14–18], the mobility may be significantly degraded in high-speed devices incorporating high fields in which the carrier temperature becomes elevated; the presence of hot carriers significantly enhances carrier–carrier scattering [19–21]; and the effect of carrier–carrier scattering on the decay of the current may become the limiting factor. In this paper, we present direct, time-domain investigations of the relaxation of electric currents in graphene due to hot carrier scattering.

Our approach is to optically inject a current using the method of coherent control with ultrashort optical pulses. The effect of hot carriers on the coherently injected electric current is studied both experimentally and theoretically via a microscopic solution of a Boltzmann equation incorporating carrier–carrier and carrier–phonon scattering. The results indicate that hot carriers are effective in damping the current, and are expected to be important for understanding the operation of high-speed graphene electronic devices.

Optical injection of a directional current in graphene is accomplished using the well-established ω–2ω coherent control technique [23–25], in which phase-correlated ~220 fs pulses at a fundamental frequency (wavelength of $3.2\,\mu$m) and its second harmonic ($1.6\,\mu$m) are simultaneously incident on the sample [22]. Quantum interference between single-photon and two-photon absorption breaks the material symmetry and the photo-injected carriers carry a net ballistic electric current as shown in figure 1(a) [23–25]. This ultrafast current radiates a single-cycle terahertz (THz) pulse with amplitude proportional to the current, and the THz pulse is measured by electro-optic (E-O) sampling in the far field [22, 24]. This all-optical current generation and detection scheme requires no electrical contacts and thus avoids the effects of parasitic resistance or capacitances.

The sample utilized in this work is a multilayer epitaxial graphene film produced on the C-terminated face of single-crystal 4H-SiC by thermal desorption of Si [26–28]. The sample has about 63 layers; most experimental evidence indicates that the layers in C-face epitaxial graphene are essentially decoupled electronically, so the electronic structure governing the transport is effectively that of single-layer grapheme [29]. We have recently shown that
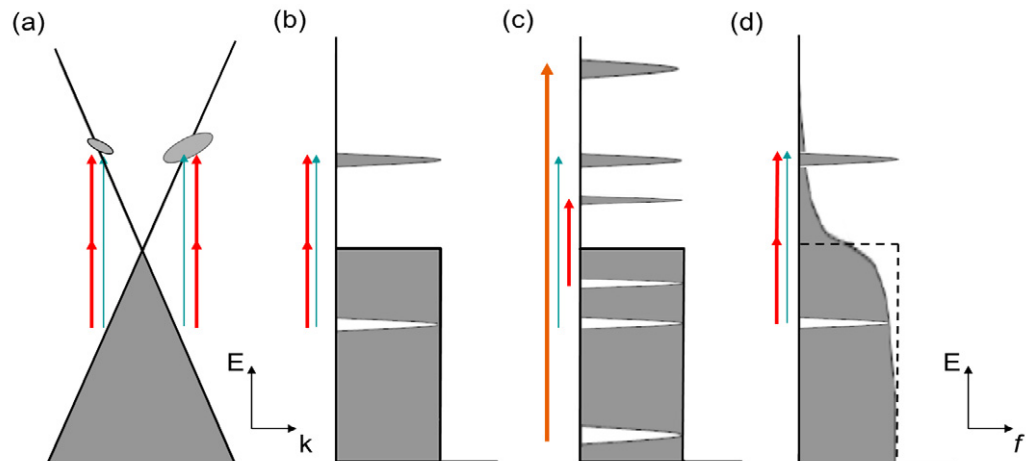
Figure 1. Schematic diagram. (a) Energy dispersion diagram of an undoped graphene layer under the excitation of phase-related fundamental and second-harmonic pulses to generate coherently controlled photocurrent. (b) Electron–hole distribution from coherently controlled fundamental and second-harmonic pulse excitations. (c) Excitation of thermal background of hot carriers due to one-photon transition of a fundamental pulse and 800 nm prepulse excitation. (d) Coherently controlled photocurrent generation under a thermal background of hot carriers injected by both a 800 nm prepulse and one-photon transition of a fundamental pulse after thermalization via electron–electron scattering.

coherent control experiments indicate the presence of some electronic coupling [30], although this coupling is not expected to affect the scattering physics considered in this paper. The bottom graphene layer is heavily doped and the doping density decreases to nearly zero with a screening length of one layer, so most layers in the stack are nearly undoped [31]. It should be noted that there is a significant difference between coherently controlled photocurrent generation in the undoped graphene layers versus semiconductors: in a semiconductor, the one-photon absorption of the fundamental pump beam can be tuned to be forbidden due to the presence of a bandgap [23–25]. In graphene, however, the fundamental pump beam can generate electron–hole pairs in the undoped graphene layers, as shown in figures 1(b) and (d); following rapid electron–electron scattering, this becomes a thermal background of hot carriers [31].

In order to study the effect of a hot thermal background of carriers on the coherently injected current in a controlled way, we designed the prepulse experiment shown in figure 1(c): we pre-inject a hot carrier background using a prepulse at a variable (negative) delay relative to the arrival of the two-color coherent control pulses. After initial fast thermalization via electron–electron scattering, the injected hot carriers form a hot thermal distribution as shown in figure 1(d). Because the hot carriers cool on a picosecond time scale due to electron–phonon coupling, we can vary the hot carrier background temperature at the time of photocurrent generation by changing the delay between the prepulse and the two-color coherent-control pump excitation. This provides a way to study the effect of thermal background of electrons with electron temperature $T_e > 300$ K on the coherently controlled photocurrent generation. At the same time, the hot carrier temperature at various delays can be independently monitored
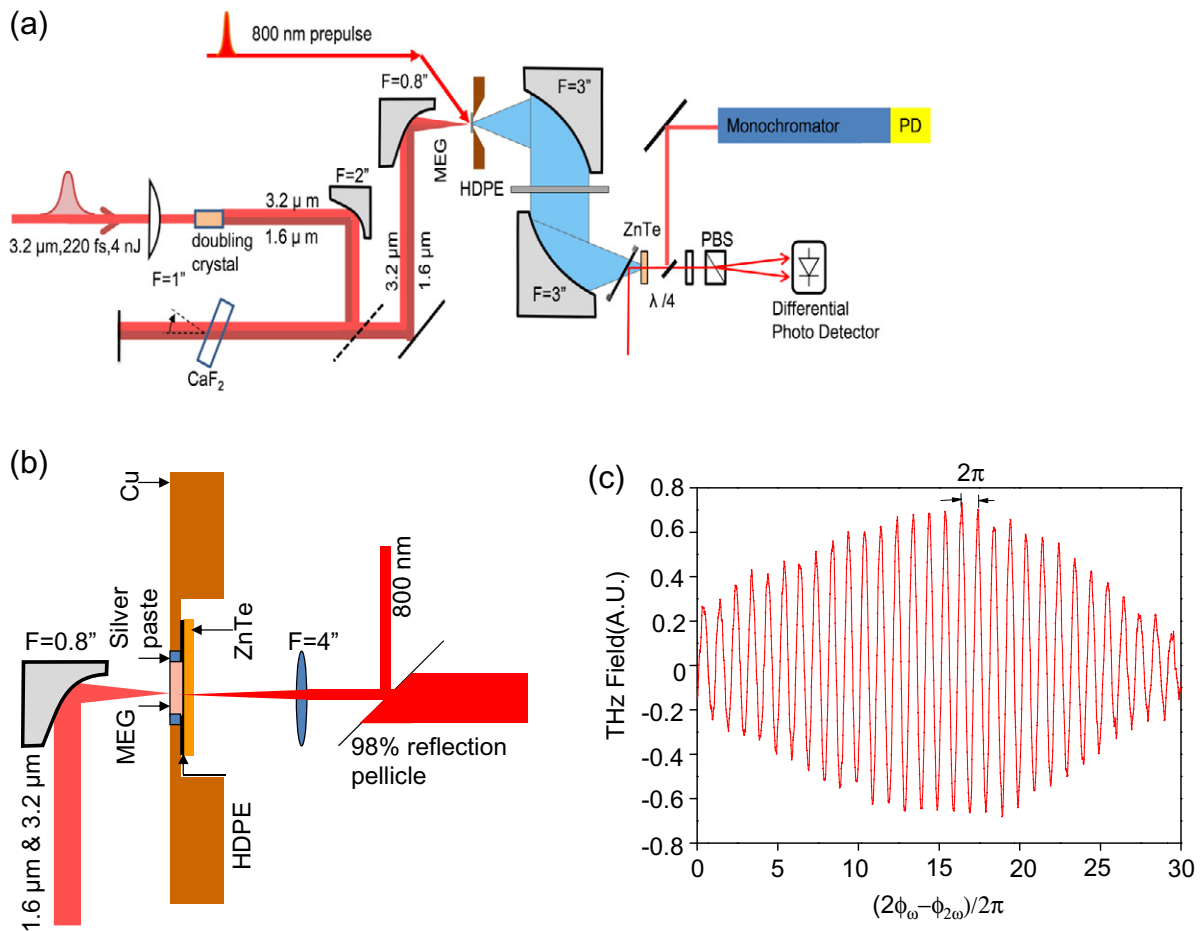
Figure 2. Experimental setup. (a) Experimental setup for prepulse experiments with far-field THz detection and *in situ* pump–probe measurement. (b) Schematic diagram for the near-field detection of the THz signal emitted by the coherently controlled ballistic photocurrent. (c) THz peak field as a function of the phase between fundamental and second-harmonic pulses.

by performing an *in situ* pump–probe experiment (using the 800 nm prepulse as the pump and either the fundamental or second-harmonic middle-infrared (mid-IR) pulse as the probe) [32].

The setup of the experiment for coherently controlled photocurrent generation with prepulse excitation is shown in figure 2(a) [22]; a commercial 250 kHz Ti:sapphire oscillator/amplifier (Coherent RegA) operating at 800 nm is used to pump an optical parametric amplifier (OPA), followed by a difference-frequency generator (DFG) to generate 200 fs pulses with 2–3 mW power at 3.2 μm (ω beam). The fundamental beam is doubled in an AgGeS$_2$ crystal to 1.6 μm with 10% conversion efficiency. The two collinear beams are either passed through a 1.5 mm CaF$_2$ plate with tunable tilt angle to adjust their relative phase, or they are separated by a dichroic mirror and enter the two arms of a Michelson interferometer; one arm of the Michelson has a piezostage that can modulate the relative length between the arms, thus controlling the relative phase between the fundamental and second-harmonic pulses. The beams are overlapped on the sample with a 30 μm diameter (full-width at half-maximum)

spot size, producing peak focus irradiation intensities for the 3.2 and 1.6 μm beams of 2.26 and 0.32 GW cm^{-2} after the loss of all intermediate optics. The remnant 800 nm beam from the OPA is split into two arms: one is used for the sampling detection of the emitted THz radiation from of the generated photocurrent; the other is used as a prepulse to excite a hot carrier background before the arrival of the two-color coherent control beams with variable delay. The THz detection is performed using a standard E-O sampling setup with a 1.0 mm thick [110] ZnTe crystal, primarily limited by the phase mismatch between the THz and the probe beams; the effective bandwidth of the E-O detection system is estimated to be $\sim$2 THz. A flip mirror is added immediately following the ZnTe crystal to direct the transmitted mid-IR pulses to the spectrometer for an *in situ* pump–probe measurement. The signal-to-noise ratio obtained using E-O detection allows us to detect coherent control signals from samples with at least ten layers; the application of this technique to monolayer and bilayer samples will require improved detection.

In order to study the effect of a thermal background of electrons with electron temperature $T_e < 300$ K, it is necessary to cool the sample in a cryostat; in this case the emitted THz must be detected in the near field of the sample, as the mid-IR cryostat windows in our liquid helium continuous flow cryostat are opaque in the THz spectral region. The near-field detection geometry setup is shown in figure 2(b); a 100 μm high density polyethylene (HDPE) slab is sandwiched between the graphene sample on its 400 μm SiC substrate and the 0.5 mm thick [110] ZnTe crystal to block the mid-IR pulse while allowing the generated THz to go through to the E-O sampling crystal. It is necessary in near-field detection that the sampling beam does not pass through the sample, as it would generate hot carriers and influence the signal to be measured. Hence a reflection beam geometry is designed for the sampling beam: the ZnTe crystal is coated with 800 nm high-reflection coating ($>$98%) on one side what is in contact with HDPE and an 800 nm antireflection coating ($<$2%) on the other side; high-reflection coating effectively suppresses the generation of hot carriers by the 800 nm sampling beam. In order to overcome the poor thermal conduction of HDPE and provide a good heat sink to the cold finger, silver paste was filled in between both sides of the multilayer epitaxial graphene (MEG) sample and the copper holder.

With HDPE, the optical rectification signal is greatly suppressed, but it does not completely eliminate it. To completely remove the optical rectification signal, we employed phase modulation between the fundamental and second-harmonic beams. In this configuration, the length of one arm of the Michelson is modulated periodically ($\sim$90 Hz) using a piezostage with an amplitude corresponding to half oscillation period, so that the coherent control signal is modulated between the maximum and the minimum as shown in figure 2(c); this signal is detected by the lock-in amplifier locked at the oscillation frequency of the piezostage. The optical rectification signal, however, is a constant, and does not change with the phase modulation, so the optical rectification signal is completely eliminated.

The principal experimental results of this work are shown in figure 3. When a 100 fs prepulse at 800 nm excites hot carriers, the THz emission from the coherently controlled ballistic current is suppressed. At zero time delay (800 nm and coherent control pulses simultaneously incident), the THz emission decreases by as much as 60% compared to no prepulse excitation. For larger negative prepulse delays, the amount of THz reduction is smaller, and within a few picoseconds the carriers injected by the prepulse have essentially no effect on the coherent current injection. On the same plot, we show the differential transmission (DT) of both the fundamental (3.2 μm) and the second-harmonic (1.6 μm) mid-IR pulses due to the 800 nm
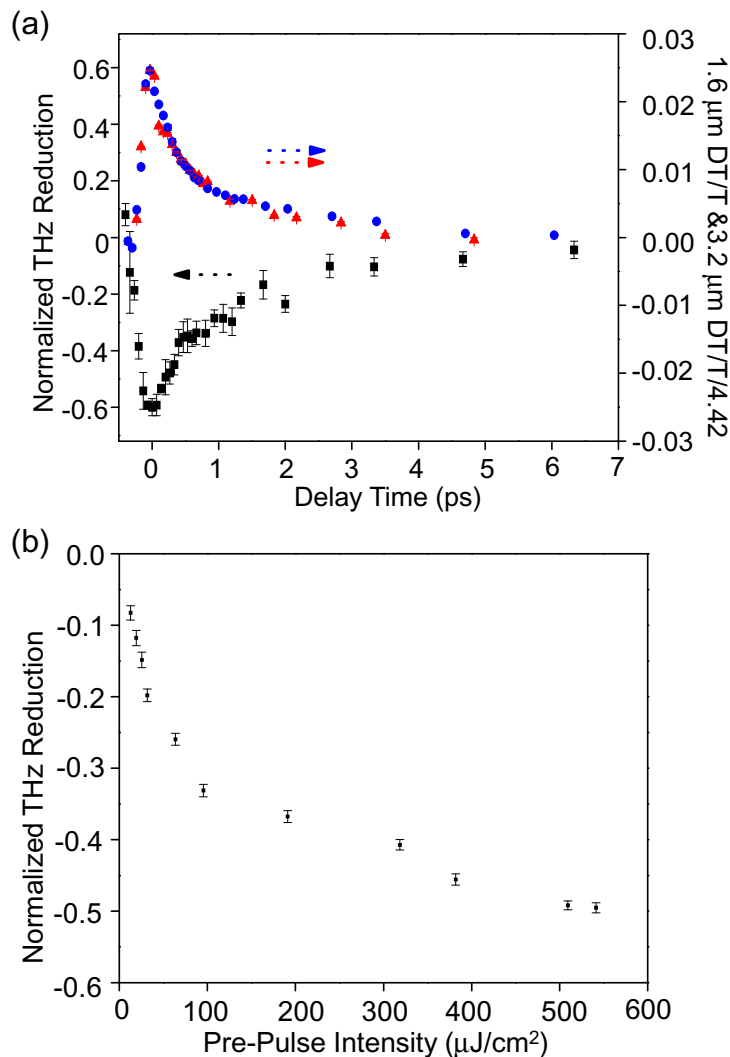
Figure 3. Prepulse reduction and *in situ* DT normalized coherently controlled THz emission reduction due to the prepulse excitation at different delays (black) and *in situ* pump–probe DT signal with a 800 nm pump (with prepulse) and a 3.2 μm (blue)/1.6 μm (red) probe. The peak DT signal at 3.2 μm is normalized with the peak of 1.6 μm. The prepulse power is 20 mW focused on a 120 μm diameter spot which converts to a prepulse intensity of 700 μJ cm^{-2}. (b) Normalized peak reduction of THz emission at time zero with different prepulse excitations.

prepulse; the mid-IR DT essentially measures the carrier temperature, and the few-picosecond decay is characteristic of carrier cooling due to electron–phonon interactions [32]. The dynamics of both the carrier cooling and the coherent current suppression are very similar, providing strong evidence that the scattering of the coherently injected electrons with the hot carrier background is primarily responsible for the current damping. Additional evidence for this interpretation is given in figure 3(b), showing the dependence of the THz suppression on the prepulse power at zero time delay: as the prepulse power increases, the background hot electron temperature at time zero increases and thus the reduction in THz emission increases.

The normalized THz reduction scales almost linearly with prepulse excitation below $100 \, \mu\text{J cm}^{-2}$ (injected carrier density of $\sim 9 \times 10^{12} \, \text{cm}^{-2}$ per layer) and reaches saturation at higher excitation power. This is partly due to the increased electron heat capacity at high temperature.

We note that, in addition to damping of the current by carrier–carrier scattering, several other mechanisms may contribute to the reduction of the THz signal induced by the prepulse: one is an increase of the THz absorption due to photoinjected hot carriers [33]; a second is Pauli blocking of the coherent-control optical transitions [32]. The first contribution has been carefully measured in an 800 nm pump and THz probe experiment with the same excitation intensity on the same sample (see supplementary information, available at stacks.iop.org/NJP/14/105012/mmedia). We find that the hot-carrier-induced THz absorption contributes not more than 45% of the measured total THz reduction at time zero. The second contribution arises from occupation of the ω–2ω optically coupled states by the background hot carriers. The *in situ* pump–probe experiment with $1.6 \, \mu\text{m}$ probe (figure 3(a)) shows that Pauli blocking contributes not more than 5% of the total reduction of THz emission at time zero. We thus estimate that not more than 50% of the THz reduction at time zero is due to the combined hot-carrier-induced THz absorption ($<45\%$) and Pauli blocking ($<5\%$). An additional mechanism potentially contributing to the THz signal reduction is space charge, i.e. the background hot carriers may dynamically screen the generated THz field [34, 35]. At present, we do not have a theory that can account for this effect. We shall see below that the magnitude of the observed THz reduction can be accounted for by the enhanced scattering by hot carriers of the coherently controlled photocurrent.

As a further check on our interpretation, we investigated the lattice temperature dependence of the coherent control THz signal amplitude; as seen in figure 3(a), the THz amplitude is essentially constant down to 10 K. This may be understood within the picture presented above, where the damping of the current is determined by the background carrier temperature; the key point is that one-photon absorption of the fundamental (ω) pulse generates an unavoidable hot carrier distribution since graphene has no bandgap, and the coherently injected current scatters from this population. The temperature of the one-photon-excited hot carrier background is determined simply by the energy absorbed from the ω pulse, and is thus completely independent of the lattice temperature. This picture is verified by the theoretical simulation shown in figure 5(b).

An additional manifestation of the carrier–carrier scattering on the THz generation is observed in the dependence of the THz amplitude on the 2ω beam power, as shown in figure 4(b). Since the coherently controlled photocurrent generation is a third-order nonlinear process, the generated current is determined by $I \sim |E_\omega|^2 |E_{2\omega}| \sim |P_\omega||P_{2\omega}|^{1/2}$ [22], so the emitted THz signal from the injected photocurrent should be proportional to $|P_{2\omega}|^{1/2}$ for fixed $|P_\omega|$. We verified that this power dependence is strictly followed when probing the third-order nonlinear tensor of ZnTe crystal with $1.6 \, \mu\text{m}/3.2 \, \mu\text{m}$ as shown in figure 4(b) (for details see the supplementary information). However, the same experiment on graphene deviates from $|P_{2\omega}|^{1/2}$ as it begins to saturate at high power. This indicates that the unbalanced one-photon absorption of the second-harmonic beam is generating a thermal background of carriers which can effectively reduce the THz emission, and this reduction is higher at higher pump excitation intensity when the carrier background is hotter.

These interpretations of the experimental results are confirmed by microscopic calculations implemented within the density matrix formalism [36]. We derive the graphene Bloch equations
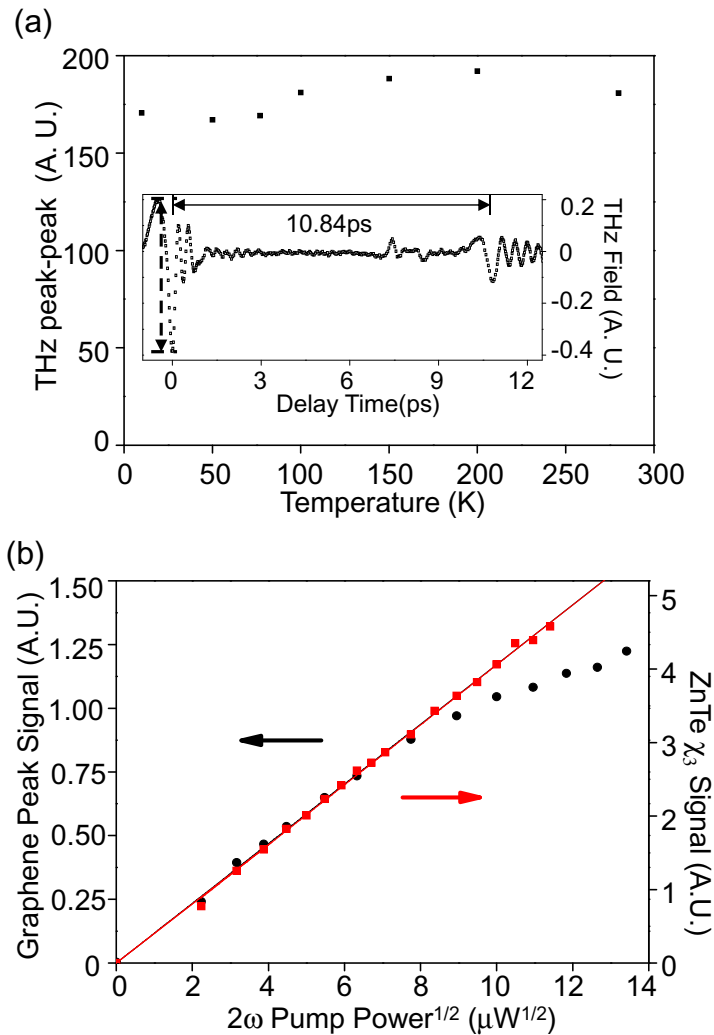
(a)

(b)

Figure 4. Temperature and power dependence. (a) Temperature dependence of the THz peak to dip amplitude (marked by the arrow in the inset) at 10, 50, 77, 100, 150, 200 and 280 K. Inset: typical time scan of the near-field detected coherent control signal. (b) The 1.6 μm pump power dependence of peak THz emission from coherently controlled photocurrent on MEG (black) and the third-order nonlinear effect (χ_3) on the ZnTe crystal (red).

describing the coupled dynamics of the carrier occupation, transition probability and phonon occupation of different optical and acoustic modes [37]. The Coulomb and the carrier–phonon interactions are considered within the second-order Born–Markov approximation, resulting in a kinetic scattering equation with explicit time- and momentum-dependent scattering rates [38, 39]. The light–matter interaction and the current are treated within the pA approach [36], as shown in detail in the supplementary material: in addition to the interband light–matter coupling, we also take into account the intraband contribution, which enables two-photon absorption. Due to the linear bandstructure, the intraband current is determined by the direction of the carrier distribution in reciprocal space. Therefore and in contrast to parabolic systems, a damping of
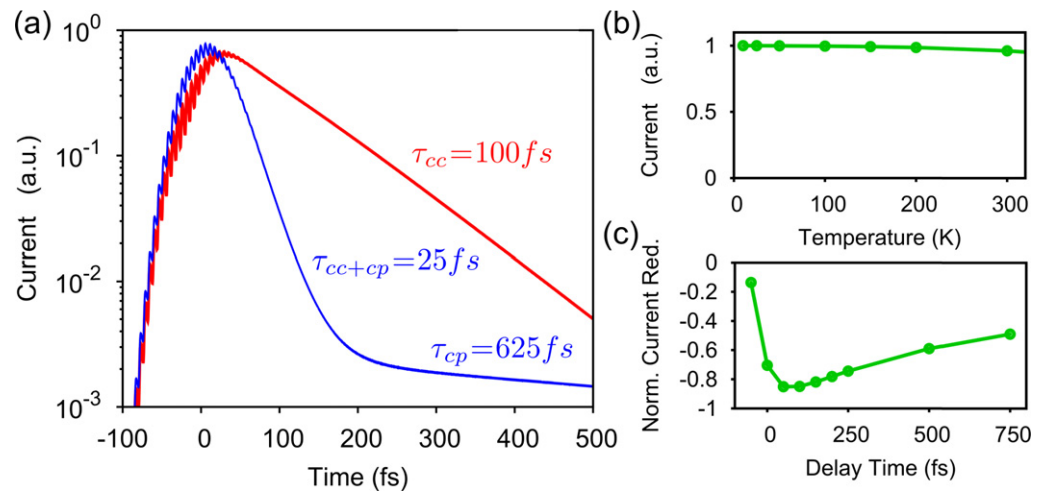
Figure 5. Theoretical simulation. (a) Theoretically calculated generation and decay of an optically injected current. The buildup adiabatically follows the exciting fields. Carrier–carrier scattering alone results in a decrease of the current with a decay constant of 100 fs (red line). The additional inclusion of carrier–phonon scattering (blue line) yields a decline characterized by two time constants: an initial ultrafast decay (25 fs) and a subsequent slower range of 625 fs. (b) The maximal current amplitude shows almost no temperature dependence for $T < 300$ K. (c) The normalized deduction of the maximal current amplitude is directly correlated to the number of pre-injected carriers.

the current corresponds to orientational relaxation of graphene's electrons, where carrier–carrier scattering is a possible relaxation channel.

The generation of a current as shown in figure 5(a) corresponds to an anisotropic carrier distribution excited by combined optical inter- and intraband transitions [39]. Its increase is step-like, since the build-up of the asymmetric carrier distribution follows adiabatically the interference contribution $I(t)$. The observed oscillations with the frequency 2ω are far above the THz regime and have therefore no influence on the experimental detection. After the pulses are switched off, the current declines and the corresponding decay channels are studied by comparing the pure Coulomb-induced relaxation dynamics (figure 5(a), red line) with a calculation considering both carrier–carrier and carrier–phonon scattering (blue line).

The influence of phonons alone on the current damping is not considered, since the ultrafast carrier redistribution cannot be neglected in such a high density regime. In contrast, the observation of the pure carrier–carrier scattering is of interest and clearly demonstrates the efficiency of velocity nonconserving Coulomb processes, reflected by the reduction of the current on the 100 fs time scale. The additional inclusion of the carrier-phonon scattering results in a much faster decrease of the current (25 fs), since both decay channels complement each other. Furthermore, some phonon modes are known to favor cross-scattering, bringing the system toward an isotropic carrier distribution [37]. After the initial ultrafast decay, the carrier system is largely equilibrated, the Coulomb dynamics plays a minor role and the presence of hot phonons delays further dynamics. Thus, the second decay time constant of 625 fs can be attributed to phonon-induced processes alone. However, the experiments

indicate that the pure Coulomb-induced fraction of the decay scales with the total carrier density as shown in figure 3(b). To model this theoretically, we vary the thermal background temperature and investigate the maximal current amplitude; see figure 5(b). In agreement with the experiment, there is no significant dependence for temperatures below 300 K, since the thermal carrier density is more than one order of magnitude smaller than the carrier density excited by the fundamental and the second-harmonic pulse, as in the experimental figure 4(a). However, calculations at higher temperatures indicate a decrease of the current amplitude with the squared thermal fraction of the carrier density. Furthermore, we have modeled the prepulse experiment shown in figure 4 considering delay times smaller than 1 ps. In agreement with the experimental observation, the calculated current is reduced due to the pre-injected carriers, shown in figure 5(c). The normalized reduction at a certain delay time scales with the remaining pre-injected carrier density. In particular, the current qualitatively reflects the prepulse-induced change of the carrier occupation at the frequency of the fundamental pulse. (Note that at delay times of the order 1 ps or longer, the carrier distribution can be described by a single Fermi level, so the carrier density is just determined by the carrier temperature.)

In summary, we have investigated the effect of hot carriers on a coherently injected current in graphene. The effect of the hot carrier background is to reduce the current and hence the emitted THz radiation. By controlling the delay between the hot carrier generation and the coherent current injection, we have demonstrated that the current damping is determined simply by the density (or temperature) of the thermal carriers. The experimental behavior is accurately reproduced in a microscopic theory, which correctly incorporates the nonconservation of velocity into scattering between Dirac fermions. It is anticipated that this effect may be significant in electronic devices based on Dirac fermions operating at high fields and/or high frequency, as the carrier temperature may become elevated under these conditions.

Acknowledgments

References

[1] Li X, Barry E A, Zavada J M, Nardelli M B and Kim K W 2010 Influence of electron–electron scattering on transport characteristics in monolayer graphene *Appl. Phys. Lett.* **97** 082101
[2] Castro Neto A H, Guinea F, Peres N M R, Novoselov K S and Geim A K 2009 The electronic properties of graphene *Rev. Mod. Phys.* **81** 109–62
[3] Novoselov K S *et al* 2004 Electric field effect in atomically thin carbon films *Science* **306** 666–9
[4] Fu L and Kane C L 2007 Topological insulators with inversion symmetry *Phys. Rev.* B **76** 045302
[5] Hasan M Z and Kane C L 2010 Colloquium: topological insulators *Rev. Mod. Phys.* **82** 3045–67
[6] Kane C L and Mele E J 2005 Z_2 Topological order and the quantum spin Hall effect *Phys. Rev. Lett.* **95** 146802
[7] Bhapkar U V and Shur M S 1997 Monte Carlo calculation of velocity-field characteristics of wurtzite GaN *J. Appl. Phys.* **82** 1649–55
[8] Bonno O, Thobel J-L and Dessenne F 2005 Modeling of electron–electron scattering in Monte Carlo simulation of quantum cascade lasers *J. Appl. Phys.* **97** 043702

[9] Fischetti M V and Laux S E 1988 Monte Carlo analysis of electron transport in small semiconductor devices including band-structure and space-charge effects *Phys. Rev.* B **38** 9721–45

[10] Goodnick S M and Lugli P 1988 Effect of electron–electron scattering on nonequilibrium transport in quantum-well systems *Phys. Rev.* B **37** 2578–88

[11] Bonno O and Thobel J-L 2008 Monte Carlo modeling of carrier–carrier scattering in semiconductors with nonparabolic bands *J. Appl. Phys.* **104** 053719

[12] Geim A K and Novoselov K S 2007 The rise of graphene *Nature Mater.* **6** 183–91

[13] Bonaccorso F, Sun Z, Hasan T and Ferrari A C 2010 Graphene photonics and optoelectronics *Nature Photon.* **4** 611–22

[14] Xia F, Mueller T, Lin Y-M, Valdes-Garcia A and Avouris P 2009 Ultrafast graphene photodetector *Nature Nanotechnol.* **4** 839–43

[15] Mueller T, Xia F and Avouris P 2010 Graphene photodetectors for high-speed optical communications *Nature Photon.* **4** 297–301

[16] Liu M *et al* 2011 A graphene-based broadband optical modulator *Nature* **474** 64–7

[17] Lin Y-M *et al* 2010 100-GHz transistors from wafer-scale epitaxial graphene *Science* **327** 662

[18] Lin Y-M *et al* 2011 Wafer-scale graphene integrated circuit *Science* **332** 1294–7

[19] Tse W-K, Hwang E H and Sarma S D 2008 Ballistic hot electron transport in graphene *Appl. Phys. Lett.* **93** 023128

[20] Das Sarma S, Hwang E H and Tse W-K 2007 Many-body interaction effects in doped and undoped graphene: Fermi liquid versus non-Fermi liquid *Phys. Rev.* B **75** 121406

[21] Wu X, Li X, Song Z, Berger C and de Heer W A 2007 Weak antilocalization in epitaxial graphene: evidence for chiral electrons *Phys. Rev. Lett.* **98** 136801

[22] Sun D *et al* 2010 Coherent control of ballistic photocurrents in multilayer epitaxial graphene using quantum interference *Nano Lett.* **10** 1293–6

[23] Newson R W, Menard J-M, Sames C, Betz M and van Driel H M 2008 Coherently controlled ballistic charge currents injected in single-walled carbon nanotubes and graphite *Nano Lett.* **8** 1586–9

[24] Costa L, Betz M, Spasenovic M, Bristow A D and van Driel H M 2007 All-optical injection of ballistic electrical currents in unbiased silicon *Nature Phys.* **3** 632–5

[25] Hach A *et al* 1997 Observation of coherently controlled photocurrent in unbiased, bulk GaAs *Phys. Rev. Lett.* **78** 306–9

[26] Berger C *et al* 2004 Ultrathin epitaxial graphite: 2D electron gas properties and a route toward graphene-based nanoelectronics *J. Phys. Chem.* B **108** 19912–6

[27] Berger C *et al* 2006 Electronic confinement and coherence in patterned epitaxial graphene *Science* **312** 1191–6

[28] de Heer W A *et al* 2007 Epitaxial graphene *Solid State Commun.* **143** 92–100

[29] Hass J *et al* 2008 Why multilayer graphene on 4H-SiC(0001) behaves like a single sheet of graphene *Phys. Rev. Lett.* **100** 125504

[30] Sun D *et al* 2012 Evidence for interlayer electronic coupling in multilayer epitaxial graphene from polarization dependent coherently controlled photocurrent generation *Phys. Rev.* B **85** 165427

[31] Sun D *et al* 2010 Spectroscopic measurement of interlayer screening in multilayer epitaxial graphene *Phys. Rev. Lett.* **104** 136802

[32] Sun D *et al* 2008 Ultrafast relaxation of excited Dirac fermions in epitaxial graphene using optical differential transmission spectroscopy *Phys. Rev. Lett.* **101** 157402

[33] Divin C J *et al* 2009 THz carrier dynamics in epitaxial graphene *CLEO/QELS OSA Techn. Dig.* paper CMT2 (http://www.opticsinfobase.org/abstract.cfm?URI=CLEO-2009-CMT2)

[34] Rodriguez G and Taylor A J 1996 Screening of the bias field in generation in terahertz from generation from photoconductors *Opt. Lett.* **21** 1046–8

[35] Kim D S and Citrin D S 2006 Coulomb and radiation screening in photoconductive terahertz sources *Appl. Phys. Lett.* **88** 161117

[36] Rossi F *et al* 2002 Theory of ultrafast phenomena in photoexcited semiconductors *Rev. Mod. Phys.* **74** 895–950

IOP Institute of Physics Φ DEUTSCHE PHYSIKALISCHE GESELLSCHAFT

[37] Malic E *et al* 2011 Mircoscopic theory of absorption and ultrafast many-particle kinetics in graphene *Phys. Rev.* B **84** 205406

[38] Winzer T *et al* 2010 Carrier multiplication in graphene *Nano Lett.* **10** 4839–43

[39] Duc H T *et al* 2005 Mircoscopic analysis of the coherent optical generation and the decay of charge and spin currents in semiconductor heterostructures *Phys. Rev. Lett.* **95** 086606

Duc H T *et al* 2006 Temporal decay of coherently optically injected charge and spin currents due to carrier-LO-phonon and carrier–carrier scattering *Phys. Rev.* B **74** 165328